Comparison of two different ceramic electrodes based on Sb-SnO$_2$ coated with BiFeO$_3$ and Bi$_2$WO$_6$ for the photoelectrooxidation of an emerging pollutant

C. Domingo-Torner [a], V. Pérez-Herranz [a], M.C. Martí-Calatayud [a], S. Mestre [b], M. García-Gabaldón [a,*]

[a] *IEC Group, ISIRYM, Universitat Politècnica de València, Camí Vera s/n, Valencia, Spain*
[b] *University Institute of Ceramic Technology / Chemical Engineering Department, Universitat Jaume I. Castellón, Spain*

A R T I C L E   I N F O

A B S T R A C T

In this work, a comparison between novel photoanodes based on Sb-SnO$_2$ (BCE) coated with BiFeO$_3$ (BFO-BCE) and Bi$_2$WO$_6$ (BWO-BCE) was carried out. An improvement in the catalytic activity of the electrodes under light exposure was demonstrated by means of Linear Sweep Voltammetry, light pulsed chronoamperometry and Electrochemical Impedance Spectroscopy, being more notorious at current densities below 25 mA·cm^{-2} for the BFO-BCE and above 25 mA·cm^{-2} for the BWO-BCE. This improved performance was caused by an increase of the photogenerated oxidizing species. As compared with the uncoated BCE anode used without light, photo-electrooxidation tests led to improvements of around 40% in the degradation degree of norfloxacin (NOR) using both photoanodes at 8.33 mA·cm^{-2}. This improvement was also observed in the mineralization degree of the model wastewaters, with an increase of 36% and 28% at 25 mA·cm^{-2} for the BWO-BCE and BFO-BCE, respectively. The degradation and formation of subproducts was followed by ion chromatography and HPLC analysis, where some of the main intermediates were detected, allowing us to elaborate a degradation route for NOR with these novel electrodes. The Mineralization Current Efficiency (MCE), energy consumption and extent of electrochemical combustion (Φ) showed improvements with light application for both electrodes at high current densities, being the BWO-BCE the one with the highest MCE and Φ at the cost of a slightly higher energy consumption. This showed the importance of light for these electrodes and its impact in the general process performance, which can be of great advantage in future applications.

1. Introduction

In the past decades, the use of antibiotics has incredibly increased due to their importance for improving the quality of life to all living beings. This massive increase of antibiotics usage is also reflected in a greater presence of them in wastewaters, since the legal regulations for these compounds are normally not clearly defined and therefore many wastewater treatment plants (WWTPs) still lack of proper removal systems [1]. Within the countries with the greatest consumption rates of antibiotics, Spain represented a 1.9% of the total consumption in 2017, with a trend to increase up to 2,7% in 2030 [2]. Around the world, many of these antimicrobials, considered now as emerging pollutants, have been proven to have a great impact on the ecology of the affected areas due to their toxicity and capability to generate bacterial resistance [3,4],

with the subsequent health problems associated. This is the case of the antibiotics group of fluoroquinolones, such as norfloxacin (NOR), for which a relatively high bacterial resistance has been detected in Spain [5].

Therefore, there is a great need to develop new and efficient methods for removing antibiotics from the environment, since the technologies currently applied in WWTPs are generally poorly adapted to their elimination [6]. Electrochemical Advanced Oxidation Processes (EAOPs) are among the main investigated technologies for this purpose because they are environmentally friendly, thanks to the fact that they do not require the addition of hazardous reagents, as they work through the direct generation of oxidizing species (e.g. $\cdot$OH, O_2^- or SO_4^-) [7]. Boron-Doped Diamond (BDD) is one of the most used electrodes in EAOPs, because it generates high concentrations of $\cdot$OH radicals that
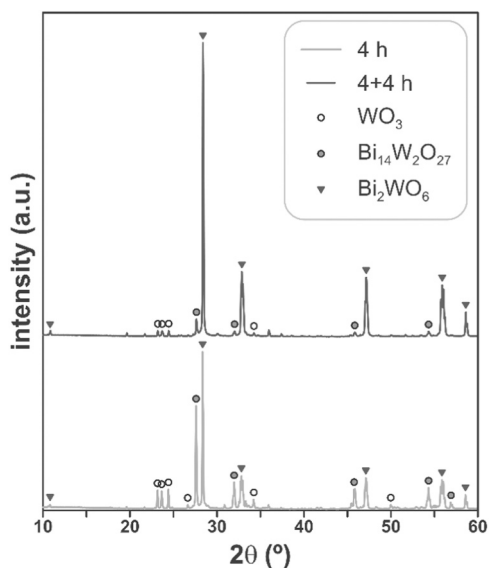
Fig. 1. Diffractograms of the two samples of catalyst synthesized with two different thermal treatments.

further react with organic pollutants, transforming them into less harmful species such as CO_2 and H_2O [7,8]. The high capability of BDD to generate $\cdot OH$ radicals is related to the fact that BDD is a non-active anode, that is, it has a high overpotential for the oxygen evolution reaction. As compared with the minimum theoretical potential for water oxidation of $1.23\ V_{RHE}$, the onset potential for this reaction in the case of non-active electrodes is normally higher than $2\ V_{RHE}$ [9].

However, the high production cost of commercial BDD electrodes [10] has motivated research studies using alternative materials with similar capabilities. Some non-active anodes that are extensively used are those based on PbO_2 or SnO_2. Pure PbO_2 has a low production cost compared to BDD and has greater electrical conductivity and stability than the pure SnO_2, but at the cost of having a lower oxygen evolution potential, which is around 1.8–2 V for the PbO_2 and 1.9–2.2 V for the SnO_2, this making the SnO_2 slightly better in terms of $\cdot OH$ generation [11,12]. Many works have proposed improvements for the pure PbO_2 in order to optimize its capabilities as an electrocatalyst, like using a bismuth-doped three-dimensional network carbon felt/PbO_2

($CF/Bi-PbO_2$), where Bi improved the oxygen evolution potential, the electrochemical active area and the service time greatly. Moreover, its capabilities in the removal of diuron herbicide were tested, achieving up to 97.6% removal in 25 min [13]. As for the SnO_2, one of its main doping improvements is the usage of Sb on SnO_2 ($Sb-SnO_2$), which is also a non-active anode that generates high quantities of $\cdot OH$. This was the material used in our previous works, over a ceramic matrix, referred to as BCE (Basic Ceramic Electrodes). BCE was compared with BDD in the degradation of NOR [14], and also, the addition of CuO to the BCE structure was tested as a strategy to reduce their electrical resistance [15]. Our latest investigation was based on coating them with photo-active materials, such as $BiFeO_3$, via dip-coating [16], in order to increase their capability to generate $\cdot OH$ radicals by photocatalytic and electrochemical means. Indeed, a noticeable improvement was noticed with a 62% mineralization of NOR under light exposure for a BCE coated with $BiFeO_3$, whereas only a 40% mineralization was achieved with the BCE. These results proved the great possibilities of improvement of the basic ceramic electrode with a photoactive coating. Light is key in these experiments because it enhances the formation of $\cdot OH$ radicals when it reaches the photocatalyst surface [17]. After the improvement observed with $BiFeO_3$, more materials based on bismuth were studied and tested, one of those is Bi_2WO_6.

Bi_2WO_6 is a photocatalytic material that has attained great attention, as it is non-toxic, it exhibits high thermal and photocatalytic properties and a low bandgap of around 2.8 eV [18–20]. It presents great photo-activity under visible light exposure thanks to its unique alternating layered structure, which allows Bi_2WO_6 to absorb radiation at longer wavelengths, which can be provided via the direct exposure to solar light [21,22]. These characteristics are achieved thanks to the properties of its components. WO_3 is not only a non-toxic component, but also it is a photostable semiconductor capable of absorbing visible light [23]. Bismuth-based materials are known by their low production cost, narrow band gap, photostability and resistance to photocorrosion [24]. Its great performance in terms of degrading different emerging pollutants has been demonstrated in different studies, for example, NOR using a ZnO/Bi_2WO_6 heterojunction [25]; dyes such as Plasmocorinth B using $Bi_2WO_6/ZnWO_4$ [26] or Rhodamine B using Bi_2WO_6 [22]; and tetracycline using a $Bi_2WO_6/CuBi_2O_4$ heterojunction [27]. Also, working with thin films of the photocatalyst over a solid support has been chosen as a promising alternative in this field [28]. For achieving these films, different techniques are available, but one of the most cost-effective and simplest techniques is dip-coating.
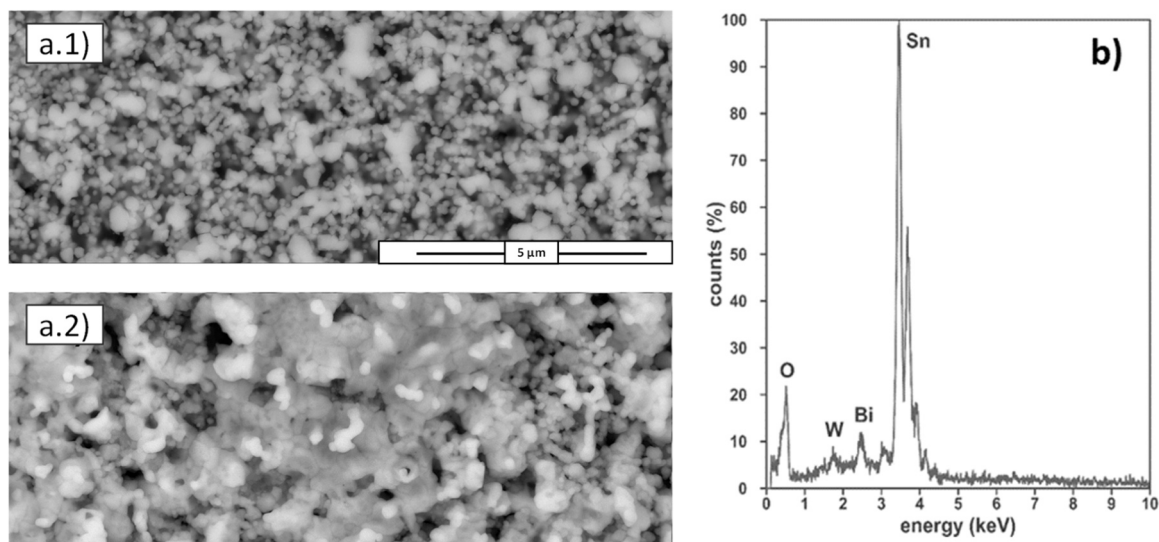

Fig. 2. (a.1) SEM image of the uncoated BCE and (a.2) SEM image of coated BCE electrode surface with the Bi_2WO_6 photocatalyst. (b) EDX analysis of the catalyst deposited in the electrode surface.
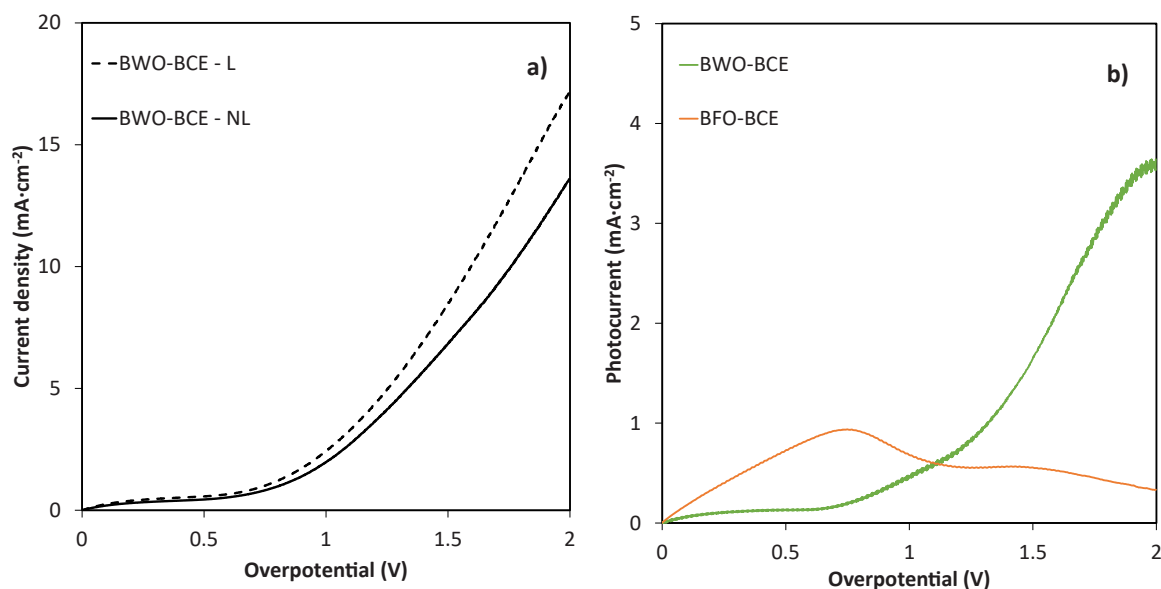
Fig. 3. (a) LSV comparison of the BWO-BCE in presence (L) and absence (NL) of light; (b) Photocurrent evolution profiles for both coatings BWO-BCE and BFO-BCE.
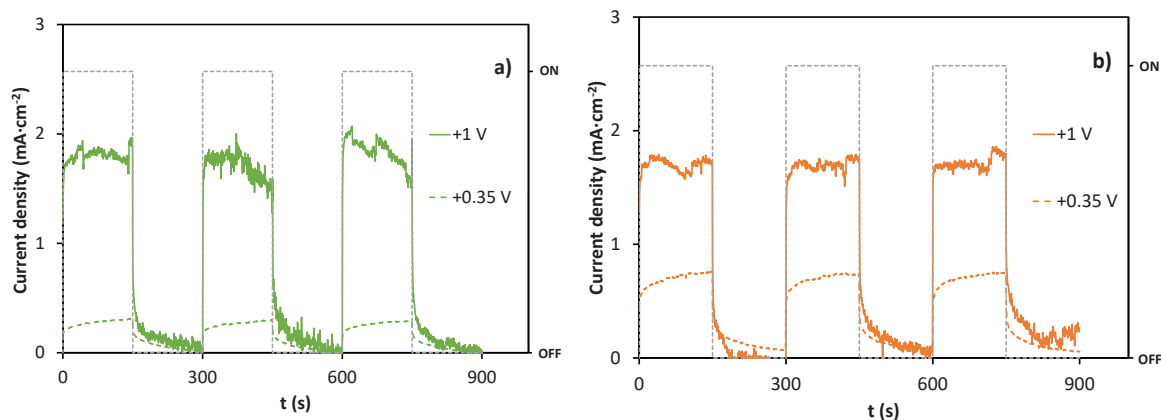

Fig. 4. Light pulsed chronoamperometry for the BWO-BCE (a) and BFO-BCE (b) electrodes for two different overpotentials, $+ 0.35$ V and $+ 1$ V.

Taking into consideration the properties and capabilities of Bi_2WO_6 as a coating for the BCE (BWO-BCE), a comparison between an already studied $BiFeO_3$ (BFO-BCE) photoanode, the new BWO-BCE one and the BCE electrode has been conducted in the present work. The aim of this study is to evaluate the capabilities of two different bismuth-based materials as photoactive coatings for cost-efficient and easy manufactured Sb-SnO_2 ceramic based electrodes that could give another perspective to the elimination of emerging pollutants. To achieve this, the degradation of NOR as a model emerging pollutant is studied.

2. Material and methods

2.1. Materials and chemicals

For the synthesis of the BWO-BCE, SnO_2 and Sb_2O_3 (purity 99.85%, Quimialmel S.A., Spain and purity 99%, Alfa-Aesar, Germany, respectively), polyvinylalcohol (PVA, Mowiol 8–88, Clariant Iberica S.A. Spain), ammonium metatungstate hydrate $((NH_4)_6W_{12}O_{39}\cdot xH_2O \geq 85\%$ WO_3, Sigma Aldrich, Germany), bismuth oxide (Quimialmel S.A., Spain) and isopropyl myristate (Quimidroga S.A. Spain) were used.

For the norfloxacin degradation experiments, analytical grade sodium sulfate (99%) from Sigma-Aldrich, norfloxacin from Cinfa (400 mg pill), sulphuric acid (96%) from J.T Baker and distilled water were used.

Persulfate analysis was performed using potassium iodide (>99%) from Honeywell, sodium thiosulfate from Sigma-Aldrich and starch solution (1%) from PanReac.

For the ion chromatography tests, a mixture of nitric/dipicolinic acid, sodium carbonate (>99%) and sodium hydrogen carbonate (>99%) from Sigma-Aldrich were used.

For the HPLC analysis, ultrapure water, LC-MS grade acetic acid from Fischer Chemical and hypergrade LC-MS acetonitrile from Merck were used.

2.2. Electrode synthesis

The electrodes were made of a solid mixture of antimony oxide in tin oxide obtained from a mixture of SnO_2 and Sb_2O_3, in a mole ratio 99/1. Polyvinylalcohol was used as a binder, which was added in a 0.8 wt% to the oxides. The processing conditions employed for the electrode synthesis was described elsewhere [29]. Briefly, prismatic specimens of $80 \times 20 \times 5$ mm were shaped by dry pressing the wet powder in a laboratory automatic press working at 250 kg·cm^{-2} (SS-EA, Nannetti Srl, Italy). The green specimens were sintered in an electric furnace (RHF1600, Carbolite Furnaces Ltd, UK). The temperature profile was heating at 5 ºC·min^{-1} from room temperature to 1200 ºC, a stage of 1 h at the maximum temperature and subsequent cooling.
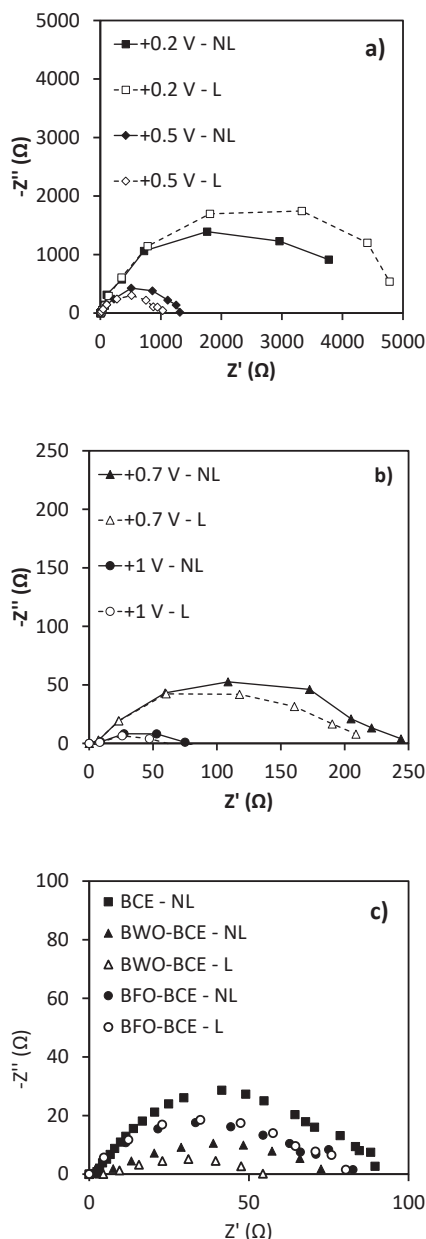
Fig. 5. EIS profile for the BWO-BCE electrode in presence (L) and absence (NL) of light applying different potentials over the OCP: (a) + 0.2 and + 0.5 V (b) + 0.7 and + 1 V; c) Comparison of EIS profiles for the BCE, BWO-BCE and BFO-BCE at 1 V over the OCP in presence (L) and absence (NL) of light.

Bi_2WO_6 was synthesized from ammonium metatungstate hydrate and bismuth oxide. Stoichiometric proportions of the raw materials were dry mixed in an agate mortar to prevent solubilization of the tungsten precursor. The reaction was performed in a mullite crucible with a porcelain lid inside the electric furnace previously mentioned. The synthesis cycle was heating at $10 \ ºC·min^{-1}$ up to 700 ºC, a soaking time of 4 h and subsequent cooling. After the synthesis, the product was ground in an agate mortar until it passed through a 200 μm mesh. The powder was then calcined again with the same heating cycle, and the product was reground in the mortar until it passed through the 200 μm mesh. This powdered product was used to prepare the catalyst suspension, milling a mixture of sieved powder and isopropyl myristate in a planetary mill with microballs (Pulverisette 5, Fritsch GmbH, Germany) for 60 min at 260 rpm. The suspension has a 0.6 wt% in Bi_2WO_6, as previous experiments showed that this ratio produced a better-quality

layer on the electrode. $BiFeO_3$ synthesis was explained in detail in our previous work [16], which shared the same synthesis procedure only varying the precursors of the photocatalyst and some heating conditions, since the Bi_2WO_6 required a higher temperature.

The deposition of the catalysts by dip-coating was carried out in a home-made apparatus, which enables the control of immersion and emersion speeds. After the deposition, the electrodes were dried in an oven and the catalyst thermally fixed with a treatment, characterized by heating at $10 \ ºC·min^{-1}$ up to 1000 ºC for the Bi_2WO_6 and 800ºC for the $BiFeO_3$, and 1 h of soaking time, in the electric furnace (RHF 1400, Carbolite Furnances Ltd. UK).

2.3. Physical characterization of the electrodes

Bulk density of the sintered electrodes was measured by mercury immersion (Archimedes method). The electrical resistivity of the sintered samples was measured by a four point method with a HIOKI RM3545 equipment (Hioki E.E. Corporation, Japan), using a homemade setup. Characterization of crystalline structures was performed using an X-ray diffractometer (Theta-Theta D8 Advance, Bruker, Germany), with CuK radiation ($\lambda = 1.54183$ Å). The generator applied an intensity light source of 45 kV and 40 mA. XRD data were collected by means of a VÅNTEC-1 detector in a 2θ from 5° to 90° with a step width of 0.015° and a counting time of $1.2 \ s·step^{-1}$. Images of the electrode surface were taken with a FEG-SEM (QUANTA 200 F, FEI Co, USA) with microanalysis (Genesis 7000 SUTW, EDAX, USA) to evaluate the characteristics and the composition of the catalyst particles.

2.4. Electrochemical characterization of the electrodes

Accelerated lifetime tests for the BCE electrode were performed in a previous work [30]. These tests were performed under $100 \ mA·cm^{-2}$ in a 0.5 M H_2SO_4 solution during 24 h using a three-electrode configuration. The reference was an Ag/AgCl electrode from Metrohm; the counter electrode was a Pt foil from Mettler Toledo and the working electrode was the BCE. Achieving potential values greater than 5 V over its initial value was considered as a deactivation of the electrode and if the electrode showed no potential variations after 24 h, the current density was increased $100 \ mA·cm^{-2}$ and the cycle was repeated several times.

For the electrochemical characterization experiments, a quartz reactor filled with a solution of 0.1 M of sodium sulfate, under a three-electrode configuration (see Fig. SM1) was employed. The reference and counter electrode were the same as in the lifetime tests, but here the working electrodes were the BCE, BWO-BCE and BFO-BCE photoanodes with an effective surface of $0.25 \ cm^2$. A PGSTAT302N Autolab potentiostat/galvanostat from Metrohm was used as a power source and to monitor the electrochemical tests.

Linear Sweep Voltammetry (LSV) was conducted at a scan rate of 50 $mV·s^{-1}$, from the open circuit potential (OCP) towards the positive direction up to an overpotential of + 2 V. A Hamamatsu Lightningcure LC8 with a 200 W Xenon lamp was used as a source of light. In order to block the infrared light, an A9616–08 light filter was inserted, which only allows the passage of radiation in the visible range.

Light pulse chronoamperometry was performed at two different overpotentials (+0.35 and +1 V from the OCP), which were selected on the basis of the LSV experiments, with a pulse duration of 150 s

Electrochemical Impedance Spectroscopy (EIS) analysis were performed in a range of overpotentials in presence and absence of light (+0.2, +0.5, +0.7 and +1 V), working with an amplitude of 5 mV and a frequency range between 10 kHz and 1 Hz.

2.5. Photoelectrochemical experiments

In the photoelectrochemical experiments, the same reactor as that employed for the characterization of the electrodes experiments was
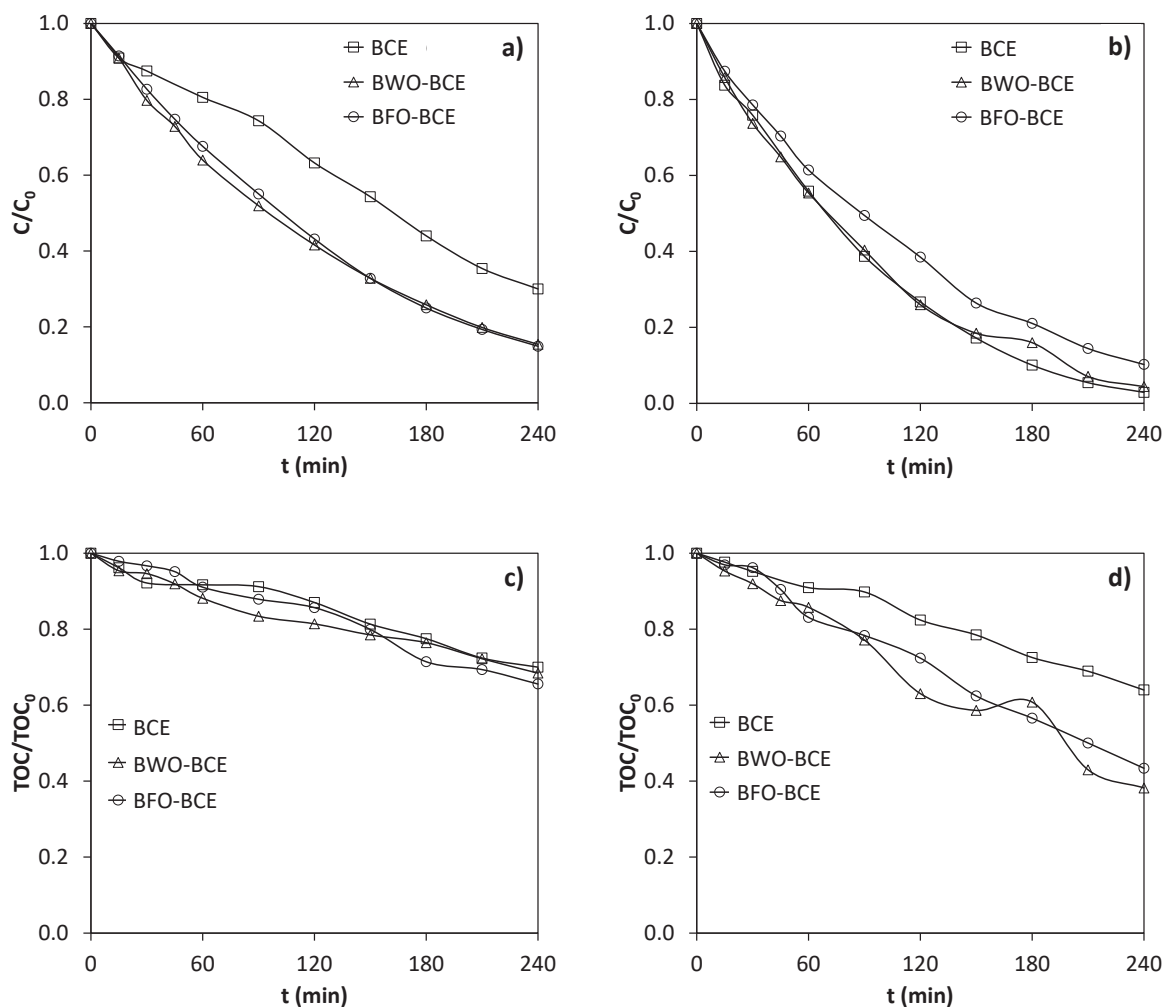
Fig. 6. Evolution of the degradation (C/C_0) and the mineralization (TOC/TOC_0) in absence of light at (a),(c) 8.33 mA·cm^{-2} and (b),(d) 25 mA·cm^{-2} for the BCE, BWO-BCE and BFO-BCE.

also used, but in this case, the solution was composed of 100 mg·L^{-1} of NOR and 2 g·L^{-1} of supporting electrolyte, Na$_2$SO$_4$. The anodes (24 cm^2) were the BCE, BWO-BCE and BFO-BCE, the reference was an Ag/AgCl from Metrohm, and the cathode was a 24 cm^2 sheet of stainless steel (AISI304). Four different current densities were studied (8.33, 16.67, 25 and 33.33 mA·cm^{-2}), under visible light exposure and without it. The light source used was the same 200 W Xenon lamp used during the electrochemical characterization. The experiments lasted 4 h and eleven samples were extracted every 15 min during the first hour of experiment and then every 30 min

2.6. Methods of analysis

The NOR concentration evolution was determined using a UV/Vis device Unicam UV4–200, following its characteristic absorption band of NOR at a wavelength of 277 nm (as shown in Fig. SM2). The mineralization of NOR was followed by measuring the Total Organic Carbon (TOC) using a Shimadzu TNM-L ROHS TOC analyzer. The ion content of the samples was analyzed using an ionic chromatograph Metrohm 883 Basic IC Plus. A iodometric titration was used to determine the persulfates of the samples [31].

For the HPLC analysis, an Agilent 1290 Infinity UHPLC equipped with a C18 column (ZORBAX Eclipse Plus) was used. The method followed is described elsewhere [16].

2.7. Assessment of the reactor performance

The mineralization current efficiency, was calculated using Eq. (1) [32,33]:

$$MCE = \frac{\Delta TOC_t}{7.2 \cdot 10^5} \frac{n}{m} \frac{F}{I} \frac{V}{t} \cdot 100\% \tag{1}$$

where ΔTOC_t is the difference of TOC concentration between a given time t and the initial value, n is the number of electrons exchanged in the reaction of complete oxidation of NOR (Eq. (2)), F is the Faraday constant (96,500 C·mol^{-1}), V is the solution volume (L), 7.2·10^5 is a unit correction factor, m is the number of carbon atoms in the NOR molecule and I is the applied electric current.

$$C_{16}H_{18}FN_3O_3 + 29H_2O \rightarrow 16CO_2 + 3NH_4^+ + F^- + 64H^+ + 66e^- \tag{2}$$

The energy consumption per kg of TOC removed (kWh·kgTOC^{-1}) was calculated making use of Eq. (3) [33,34]:

$$E = \frac{\int_0^t U(t) \ I(t) dt}{\Delta TOC_t \ V} \tag{3}$$

where $U(t)$ is the cell voltage (V).

The extent of electrochemical combustion (Φ) was calculated using Eq. (4) [31,35]:
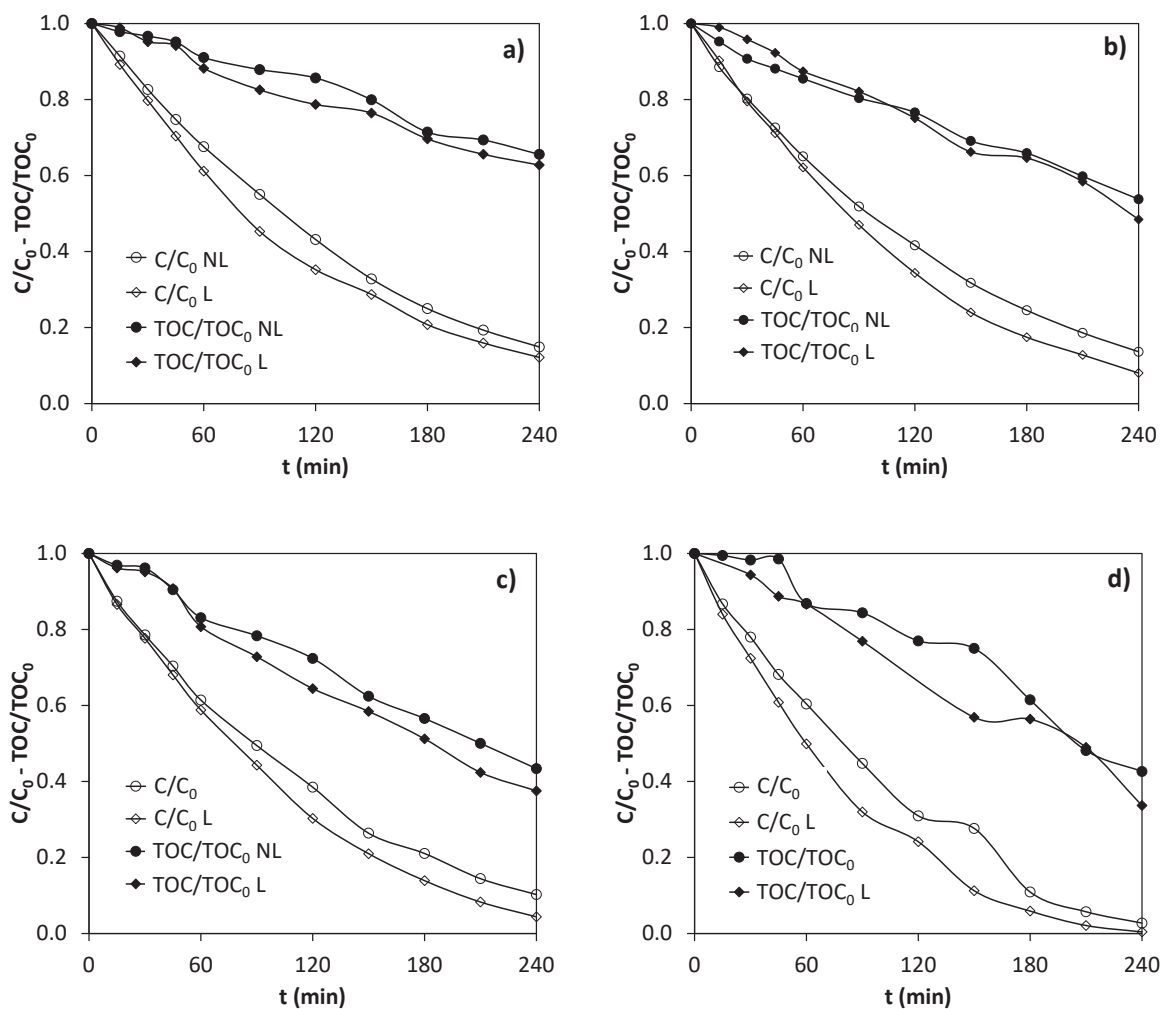
Fig. 7. Evolution of the degradation (C/C$_0$) and mineralization (TOC/TOC$_0$) in presence (L) and absence (NL) of light at (a) 8.33 mA·cm^{-2}, (b) 16.67 mA·cm^{-2}, (c) 25 mA·cm^{-2} and d) 33.33 mA·cm^{-2} for the BFO-BCE.

$$\Phi = \frac{\%TOC_{removed}}{\%NOR_{removed}} \tag{4}$$

where Φ ranges between 0 and 1 (0 means that the process takes place with oxidation but without mineralization, and 1 that there is a total mineralization of NOR).

3. Results and discussion

3.1. Electrode characterization

The sintered ceramic electrodes showed a bluish colour, an indication of the formation of the solid solution between tin and antimony oxides. This assumption was confirmed by the mean resistivity value of the samples, 0.0246 ± 0.0002 Ω·cm for the BWO-BCE and 0.0228 ± 0.0005 Ω·cm for the BFO-BCE, which were sufficiently low for the electrode function, considering their ceramic nature. Their low bulk density (mean 3691 ± 13 kg·m^{-3}) allows us to estimate a porosity of around 46% by comparison with the true density of tin oxide, very similar to the 50% porosity value obtained for the BFO-BCE.

For the BWO-BCE, the products of the two thermal treatments were yellowish and easy to grind, an indication that the densification mechanisms had low activity along synthesis. The XRD characterization indicates that, after the first thermal treatment, the product is a mixture of the target phase Bi$_2$WO$_6$ with unreacted WO$_3$ and a low proportion of another bismuth tungstate Bi$_{14}$W$_2$O$_{27}$ (4 h in Fig. 1). However, after the

second thermal cycle (4 +4 h in Fig. 1), the product had a higher proportion of Bi$_2$WO$_6$, as the reflections of Bi$_{14}$W$_2$O$_{27}$ and tungsten oxide were of reduced intensity. Consequently, the product of the second thermal treatment was selected to elaborate the catalyst suspension. Considering that there are five stable phases at room temperature in the Bi$_2$O$_3$ - WO$_3$ phase diagram [36], the synthesis of the catalyst can be considered simple. Additionally, the successful synthesis of BFO-BCE was also reported in a previous work [16]. The only difference observed among both photocatalysts was the ease to obtain a purer phase, since BiFeO$_3$ presents a really limited stability interval which complicates obtaining a pure coating of this material.

After the deposition process, the characterization of the electrode showed that the catalyst was well fixed to the surface of the BCE substrate (Fig. 2a). Specifically, the surface free of catalyst that shows its characteristic porosity is observed in Fig. 2a.1 and the catalyst was the phase that partially filled the surface porosity, as seen in Fig. 2a.2. This was confirmed by EDX analysis, since Bi and W were present in this phase (Fig. 2b), but the main signal is generated by the tin oxide of the ceramic substrate. This result implies a high compatibility between the catalyst particles and the ceramic support, which can support large amounts of catalyst per unit area.

Accelerated service life tests showed no major changes at 100 mA·cm^{-2} after 24 h (potential increased up to 2.85 V). Therefore, 200 mA·cm^{-2} were applied and after another consecutive 24 h only an average value of 3.8 V was achieved. Then 300 mA·cm^{-2} were applied for another 24 h (making a total of 72 h of electrolysis), achieving

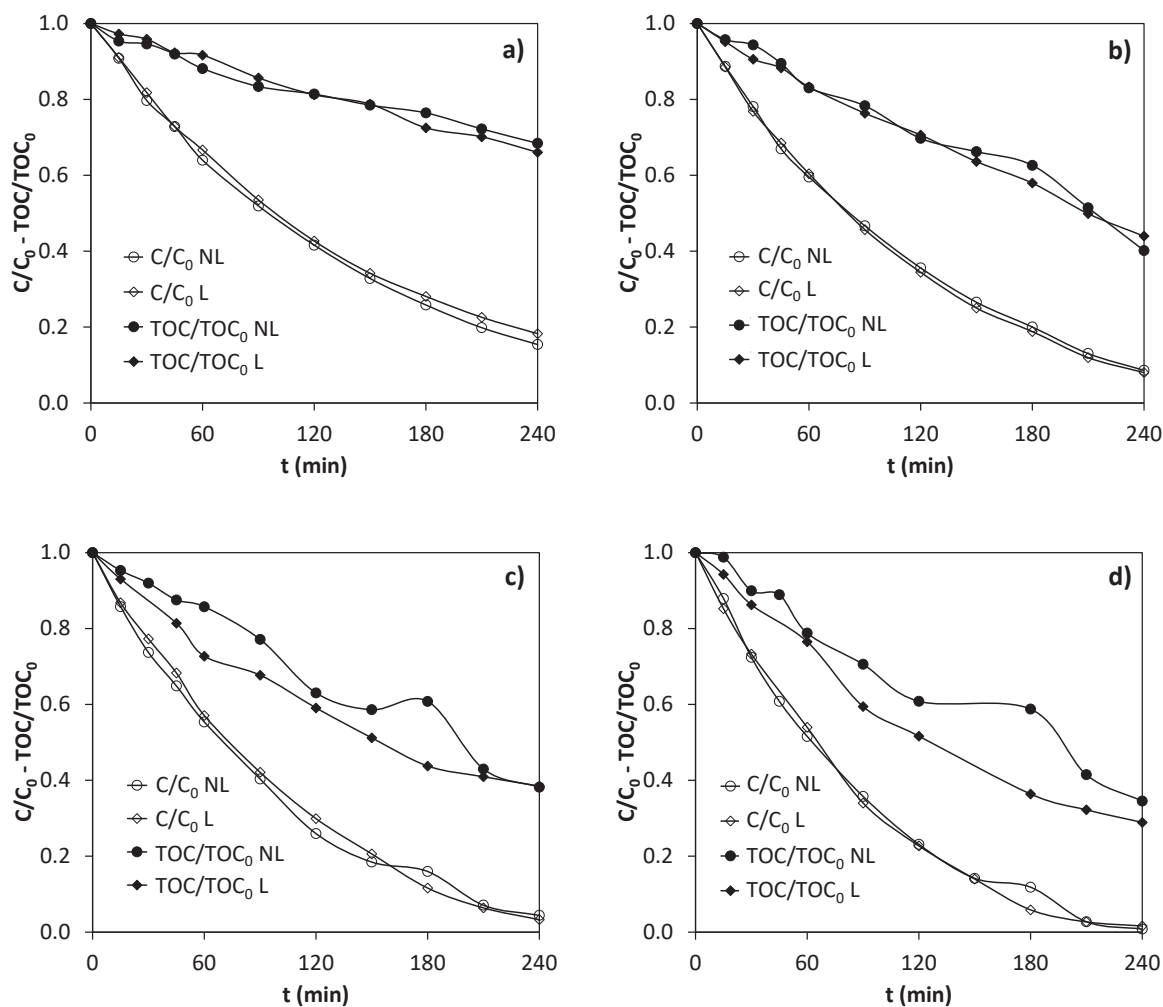**Fig. 8.** Evolution of the degradation (C/C$_0$) and mineralization (TOC/TOC$_0$) in presence (L) and absence (NL) of light at (a) 8.33 mA·cm^{-2}, (b) 16.67 mA·cm^{-2}, (c) 25 mA·cm^{-2} and (d) 33.33 mA·cm^{-2} for the BWO-BCE.

average potential values of 4.5 V. Some 5 V peaks were detected during the 200 and 300 mA·cm^{-2}, but those were related to the formation of oxygen bubbles that blocked the electrode surface. These lifetime tests, previously reported in [30] for the BCE electrode, showed no evidence of change by using SEM image analysis before and after the electrolysis.

According to the electrochemical characterization tests, similar LSV were obtained for all electrodes, as an example, the comparison between the LSV of the BWO-BCE in presence and absence of light is shown in Fig. 3a. The Bi$_2$WO$_6$ coating exhibits a limited growth of current density at low overpotentials, up to around + 0.75 V over the OCP, beyond which it follows an exponential evolution. Light increases the current density signal for the same overpotential, also having a greater effect from overpotential values of + 0.75 V onwards. This indicates that the Bi$_2$WO$_6$ coating under light exposure greatly decreases the resistance to charge transfer at higher overpotentials. This phenomenon is well observed when the photocurrent evolution is analyzed (see Fig. 3b). This figure shows the comparison of the photocurrent profiles for the BWO-BCE and the BFO-BCE. It is observed that an overpotential of around + 0.75 V there is a change in the trend: for the BWO-BCE electrode the slope changes notably, and the curve follows a clear crescent trend with the overpotential; whereas the BFO-BCE achieves a maximum of 0.94 mA·cm^{-2} at that overpotential and then a gradual decline of the photocurrent takes place. This means that the BFO-BCE works better at medium-low potentials, where its sensibility to light is higher, while the BWO-BCE works better at higher overpotential values.

Light pulsed chronoamperometry measurements at two different

overpotentials (+0.35 V and +1 V) are presented in Fig. 4. There is an instant change in the current density profile when light is applied. At + 0.35 V the 150 s pulse is necessary to achieve a steady-state value; however, at + 1 V a fairly stable value of current density is achieved almost immediately after turning on the light, but with an increased signal noise behavior due to the generation of gas bubbles. This increase in the current density under light application further confirms the photocatalytic enhancement of the BCE electrode, which is related to the higher generation of charge carriers thanks to the excitation of electrons in the valence band after light impacts the coating [37]. Fig. 4a shows the results for the BWO-BCE where, as expected from previous observations, at lower potentials, the effect of light on the photocurrent generated by the Bi$_2$WO$_6$ coating is smaller (an average value of 0.26 mA·cm^{-2}). If compared with Fig. 4b, which includes the BFO-BCE results, the BFO-BCE works noticeably better at low potentials (an average value of 0.67 mA·cm^{-2}). At higher potentials, there is no clear difference between electrodes. This confirmed the results previously seen in Fig. 3b, where at lower overpotentials, + 0.35 V, the BFO-BCE showed greater photocurrent response and at + 1 V, the photocurrent values were similar for both electrodes.

In order to further evaluate the electrochemical behavior of the BWO-BCE electrode, EIS in the presence and absence of light was performed. The results, shown as Nyquist plots, are compared in Fig. 5a and b. At lower overpotentials (+0.2 V), closer to the OCP, the effect of light does not improve the charge-transfer resistance of the system, associated to the diameter of the semicircle. As the DC potential increases (Fig. 5b),
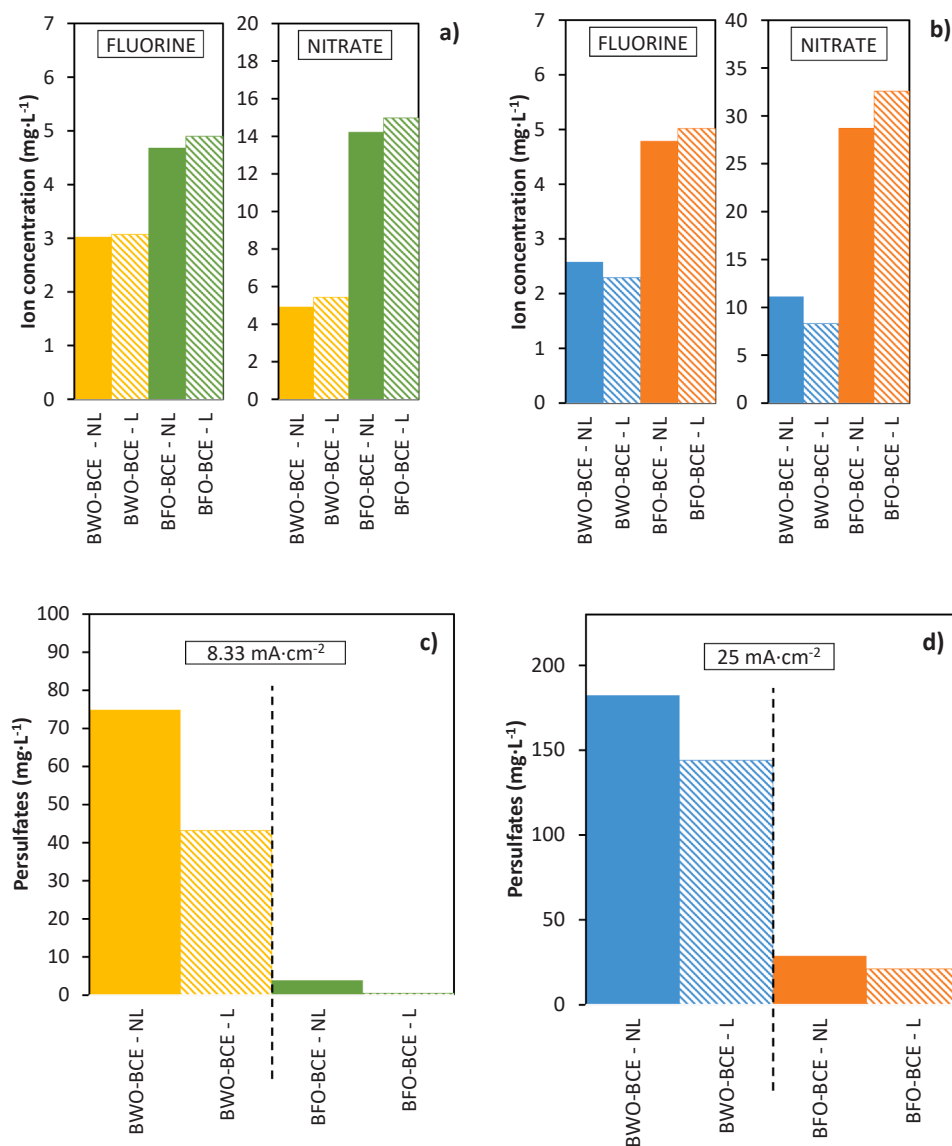
Fig. 9. Ion content of fluorine and nitrate at 240 min for the BWO-BCE and BFO-BCE at (a) 8.33 mA·cm^{-2} and (b) 25 mA·cm^{-2} in presence (L) and absence (NL) of light. Persulfate content at 240 min for the BWO-BCE and BFO-BCE at (c) 8.33 mA·cm^{-2} and (d) 25 mA·cm^{-2} in presence (L) and absence (NL) of light.

Table 1
Comparison with other works which treat antibiotics in similar conditions.

| Photoanode	Conditions	Target antibiotic	% Removal	Ref.
BFO-BCE	33.3 mA·cm^{-2}, 200 W lamp, 4 h	Norfloxacin	99% NOR 66% TOC	Current work
BWO-BCE	33.3 mA·cm^{-2}, 200 W lamp, 4 h	Norfloxacin	99% NOR 71% TOC	Current work
MMO-RuO$_2$IrO$_2$	30 mA·cm^{-2}, 9 W lamp, 7.24–8 h	Penicillin G Meropenem Chloramphenicol	82–100%	[43]
Ti/Ru$_{0.3}$Ti$_{0.7}$O$_2$	20 mA·cm^{-2}, no light, 20 min	Tetracycline hydrochloride	100%	[44]
Self-doped titanium dioxide nanotubes modified with electrodeposited Pt (SD-TNT/Pt)	25 mA·cm^{-2}, 100 W Xenon lamp, 60 min	Tetracycline hydrochloride	86%	[45]
Ti/SnO$_2$–RuO$_2$	25 mA·cm^{-2}, no light, 45 min	Cefotaxime sodium	86.33%	[46]
Ru$_{0.3}$Ti$_{0.7}$O$_2$–Ti	10.53 mA·cm^{-2}, 250 W lamp	Erythromycin	38% TOC	[47]
BiPO$_4$/Sb-SnO$_2$	15.5 mA·cm^{-2}, no light, 4 h 15.5 mA·cm^{-2}, 200 W lamp, 4 h	Norfloxacin	83.4% NOR 98.82% NOR	[48]
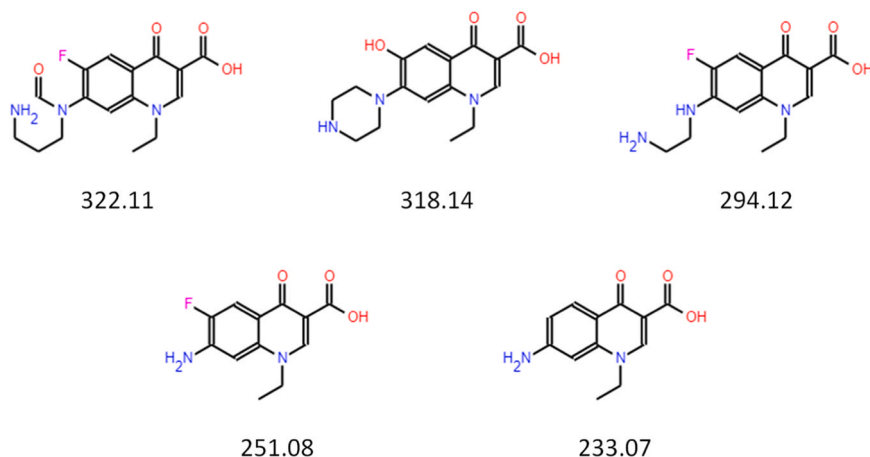
Fig. 10. By-products detected with HPLC analysis at *m/z* 322.11, 318.14, 294.12, 251.08 and 233.07.

light has a greater effect on reducing the charge-transfer resistance, confirming what was previously seen during the LSV (Fig. 3). If the influence of the applied potential is considered, it is seen that as it increases, the charge transfer resistance decreases, which is related to the inverse of the slope at the different regions included in Fig. 3a.

In Fig. 5c, a comparison of the EIS profiles at + 1 V over the OCP between the BCE, BWO-BCE and BFO-BCE is shown, where there is a clear improvement of the behavior of the coated electrodes in relation to the BCE. As expected from previous observations, the Bi_2WO_6 coating reduces the charge transfer resistance, enhancing the current flow through the electrode, which further decreases with light application, a phenomenon well observed in different photocatalysts [38]. In other words, the charge carrier transfer is enhanced when light is applied thanks to the faster generation of electron-hole pairs via incident photon collision. In addition, Bi_2WO_6 presents a better behavior than $BiFeO_3$ at higher potentials, since it presents the lowest values of charge-transfer resistance. Also, with EIS it is confirmed that light has less effect on the BFO-BCE when working at higher potentials, since its charge-transfer resistance is very similar for both cases, in presence and absence of light.

3.2. Photo-electrooxidation experiments

Fig. 6 shows the comparison of the relative concentration of NOR (C/C_0) and TOC (TOC/TOC_0) between the three different anodes in absence of light: BCE, BWO-BCE and BFO-BCE, at two different current densities. All figures follow the same evolution with time, with C/C_0 values having initially a linear descending trend up to 45–60 min and a later exponential trend until 4 h. With regards to TOC/TOC_0, the behavior observed for all the experiments follows a linear evolution through the 4 h. At 8.33 mA·cm^{-2} (Figure 6a), a clear improvement with both photocatalytic coatings is seen during the whole experience, especially in the degradation of NOR. The improvement in NOR degradation was of around 40% for both materials as compared with the BCE. In Fig. 6b the values of C/C_0 for 25 mA·cm^{-2} are shown, where there is no significant improvement with respect to the BCE with any of the bismuth coatings. In Fig. 6c, where TOC/TOC_0 at 8.33 mA·cm^{-2} is depicted, no major improvement is observed, which means that the effect on mineralization is low at these low current densities. At the higher current density of 25 mA·cm^{-2} (Fig. 6d), a notable improvement in mineralization of around 28% for the BFO-BCE and 36% for the BWO-BCE is observed, as compared with the BCE. This means that at low current densities, the bismuth coatings improve the degradation of NOR but not the mineralization, whereas at higher current densities the contrary happens. Attending to the improvements seen for both coatings a deeper analysis of the materials is shown in Fig. 7 and Fig. 8.

Fig. 7 depicts the results of the evolution of C/C_0 and TOC/TOC_0 for the BFO-BCE at the four different current densities under study in presence and absence of light. With the increase of current density, the system is faster and achieves higher degradation and mineralization rates. Values go from 85% to 88% NOR degradation at 8.33 mA·cm^{-2}, in absence and presence of light, respectively; and up to 97–99% at 33.33 mA·cm^{-2}. According to the TOC values, around 34–37% was mineralized at 8.33 mA·cm^{-2} and around 57–66% at 33.33 mA·cm^{-2}. Light had a notable effect during all experiments at all current densities within the degradation values being greater at medium current densities, as expected from Fig. 3b.

Fig. 8 summarizes the C/C_0 and TOC/TOC_0 results for the BWO-BCE at all four current densities in the presence and absence of light. With this photoanode it is also observed that with the increase of current density the system is faster, achieving values of C/C_0 at 8.33 mA·cm^{-2} of around 82–84% of eliminated NOR and increasing at 33.33 mA·cm^{-2} up to around 98–99%. A similar behavior is observed for the values of TOC/TOC_0, where at 8.33 mA·cm^{-2} about 31–34% NOR was mineralized but at 33.33 mA·cm^{-2} the value was around 65–71%. Light effect followed the same tendency as that observed during the characterization, where at low current densities the effect was lower, and it was more noticeable at higher current densities. Additionally, light seemed to have a greater effect in the mineralization but almost negligible in the degradation.

For both electrodes the observed effect of light (hυ) is accomplished thanks to the generation of electron-hole pairs (Eq. 5): electrons (e⁻) are generated in the conduction band and holes (h⁺) in the valence band [39]. During the formation of the reactive oxygen species, electrons react with O_2, reducing it and forming the superoxide radical, O_2^-, following Eq. (6); and the holes react with H_2O, oxidizing it to ˙OH as indicated in Eq. 7. The O_2^- and ˙OH radicals can react directly with the NOR molecules, oxidizing them to its subproducts as seen in Eq. 8 and Eq. 9, respectively, but also O_2^- can further react with other species generating more ˙OH radicals (Eqs. (10)−(12)). Due to the nature of the electrolyte, Na_2SO_4, there is also presence of persulfates ($S_2O_8^{-2}$) in the media, formed by direct oxidation of SO_4^{-2} ions (Eq. (13)) [40]. Persulfate ions can also become activated by the effect of light, where the electrons formed in the conduction band react with them and generate SO_4^- radicals (Eq. 14), which can directly degrade the NOR molecule or can be involved in the formation of other oxidizing species (Eqs. (15)−(17)) [41,42].

Taking these reactions under consideration, the reason why in Fig. 8 light affected more the mineralization in the BWO-BCE than in the degradation can be related to the amount of persulfate content detected (Fig. 9c), which is also later discussed. For the BWO-BCE, persulfate content is much higher than the BFO-BCE after 4 h of essay, but in presence of light it is almost reduced by a 44% at 8.33 mA·cm^{-2} and
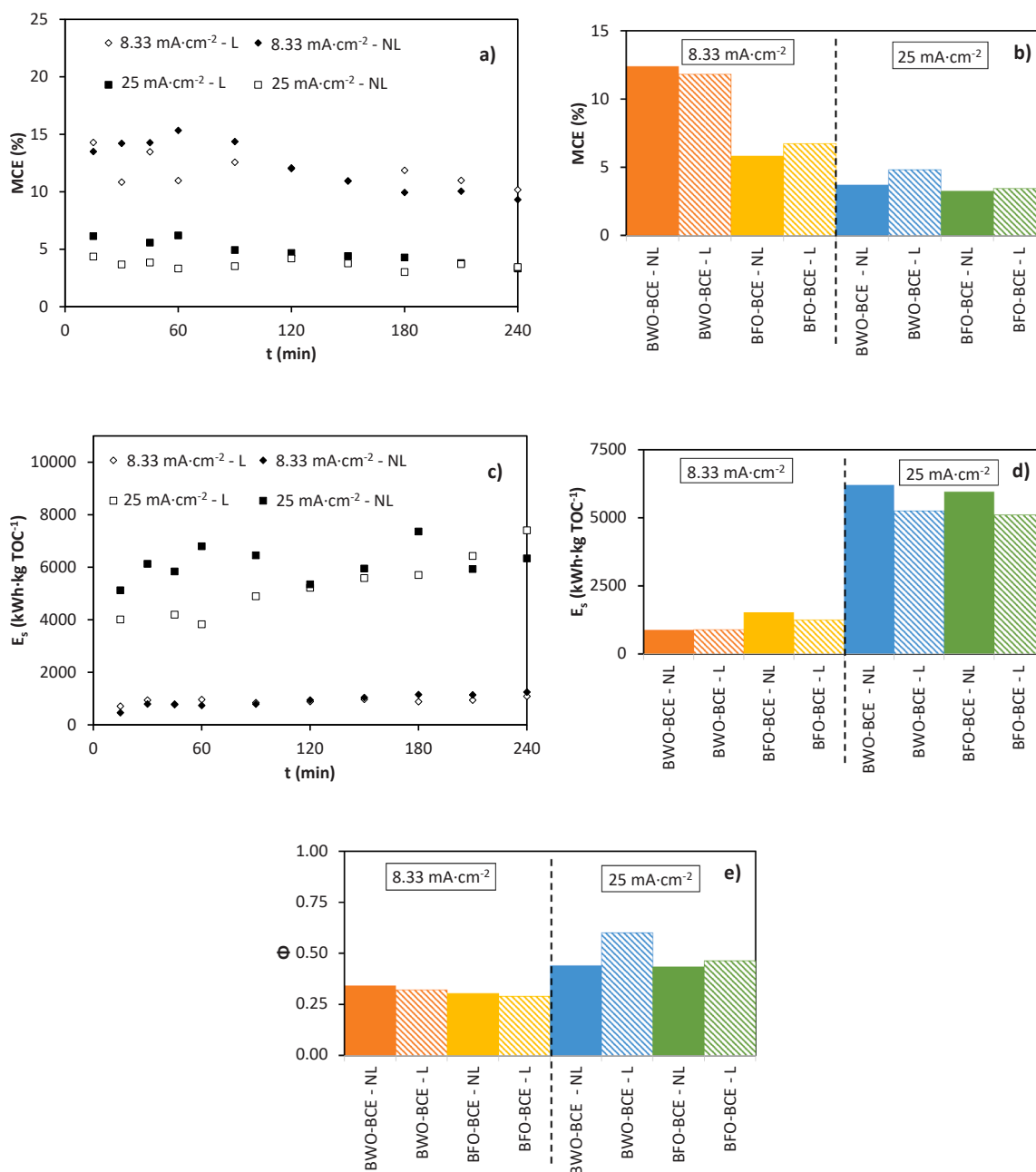
Fig. 11. Instant values of (a) MCE and (c) E_s for the BWO-BCE; Average values of (b) MCE, (d) E_s and (e) Φ for both electrodes at 8.33 mA·cm^{-2} and 25 mA·cm^{-2} in presence (L) and absence (NL) of light.

25% at 25 mA·cm^{-2}. This decrease of persulfates is related to their activation into sulfate radicals (later detailed in Eq. (14)), which are really reactive. These sulfate radicals mineralize not only the NOR molecule but also all its intermediates. Additionally, they can further create more hydroxyl radicals too (Eq. (17)).

This could be the reason why under illumination, the effect on mineralization is more noticeable, since it is always easier to oxidize a smaller molecule than the original molecule of NOR.

$$BWO - BCE + hv \rightarrow e^- + h^+ \tag{5}$$

$$O_2 + e^- \rightarrow O_2^{\cdot -} \tag{6}$$

$$H_2O + h^+ \rightarrow {}^{\cdot}OH + H^+ \tag{7}$$

$$NOR + O_2^{\cdot -} \rightarrow NOR_{subproducts} \tag{8}$$

$$NOR + {}^{\cdot}OH \rightarrow NOR_{subproducts} \tag{9}$$

$$O_2^{\cdot -} + H^+ \rightarrow HO_2^{\cdot} \tag{10}$$

$$2HO_2^{\cdot} \rightarrow H_2O_2 + O_2^{\cdot -} \tag{11}$$

$$O_2^{\cdot -} + H_2O_2 \rightarrow {}^{\cdot}OH \tag{12}$$

$$2SO_4^{\cdot -2} \rightarrow S_2O_8^{-2} \tag{13}$$

$$S_2O_8^{-2} + e^- \rightarrow SO_4^{\cdot -} + SO_4^{-2} \tag{14}$$

$$S_2O_8^{-2} + H^+ \rightarrow HS_2O_8^- \tag{15}$$

$$HS_2O_8^- + e^- \rightarrow H^+ + SO_4^{\cdot -} + SO_4^{-2} \tag{16}$$

$$SO_4^{\cdot -} + OH^- \rightarrow {}^{\cdot}OH + SO_4^{-2} \tag{17}$$

In order to compare the previous results with those obtained in other works, a comparative table (Table 1) has been elaborated, grouping data from different works that share similar conditions, showing the great behavior of the BFO-BCE and BWO-BCE in terms of the antibiotic degradation.

The formation of NOR subproducts was also followed by ion chromatography, as summarized in Figure SM3 for the BWO-BCE. Formate concentration was higher at 8.33 mA·cm^{-2} as seen in Figure SM3a due to the lower mineralization capability at lower current densities, which leads to an accumulation of short string carbon molecules. With the increase of current density (25 mA·cm^{-2}), the oxidation power increases and the accumulation of formate was significantly lower. When the effect of light is studied, for 8.33 mA·cm^{-2} the concentration of formate remains invariable confirming the low effect of light seen during the TOC analysis (Fig. 8a), but as expected at 25 mA·cm^{-2} the effect of light was greater as seen in Fig. 8c. Ammonia was followed in Figure SM3b. Initially, in absence of light there is a gradual formation of ammonia, where the concentration keeps increasing with time at both current densities up to an almost steady-state value. At 25 mA·cm^{-2} the amount achieved was greater, due to a faster degradation of the NOR molecule as seen in Fig. 8c and, therefore, a greater formation of nitrogen species takes place. In presence of light there is a notable change, where after an initial formation of the ammonia, it starts to disappear faster at 25 mA·cm^{-2} due to its oxidation towards nitrates.

Other ions, like fluoride and nitrates were also followed by evaluating their final values after 4 h. Fig. 9a shows the results at lower current densities (8.33 mA·cm^{-2}), where the content of fluorine is quite similar in presence and absence of light for both electrodes. For nitrate content, it is observed that at 8.33 mA·cm^{-2} in presence of light the amount of nitrate for the BWO-BCE is higher than in absence of light, which is due to a greater generation of radicals, which oxidize the nitrogen present in the NOR molecule leading to its accumulation. In Fig. 9b, the results at 25 mA·cm^{-2} are shown, and for both ions and electrodes the trend with light stays the same, being the main difference the amount of nitrates present in the final samples, since the concentration is doubled for both electrodes at high current densities due to a greater degradation of the NOR molecule and, therefore, a greater generation of nitrogen species.

When comparing both electrodes, the BFO-BCE generated a greater amount of fluoride and nitrate at both current densities than the BWO-BCE, which is possibly associated with the existence of variations in the degradation pathways that increase the formation of intermediates with the nitrogen and fluoride still attached to a large organic molecule.

Persulfate content for both electrodes was also followed in Fig. 9c and d. Here the influence of current density is clear, the higher the current density is (Fig. 9d), the greater the oxidation and therefore there is an increase of the persulfate content. When light is applied, persulfate content decreases in every scenario due to the activation of persulfates with light, that transforms them into SO$_4^{\cdot -}$ radicals that work as heavy oxidizing species of the NOR molecule, as previously stated. When the results of the BWO-BCE are compared with those obtained for the BFO-BCE, it is shown that the BWO-BCE generated much more persulfates. Also, since persulfates are associated to a higher toxicity of the solution, these results indicate that the BWO-BCE generates more toxicity during the degradation, and, therefore, that light reduces this toxicity due to lower persulfate generation.

With the HPLC analysis it was possible to detect some of the major subproducts from the degradation of the NOR molecule, at the following *m/z* values: 322.12, 318.14, 294.12, 251.08 and 233.07 (Fig. 10), present in the degradation route (Fig. SM4) of the NOR molecule that has been described in different studies [16,49,50]. The evolution with time of these subproducts is described in Figure SM5. The subproduct 322.11 is an early compound derived from the degradation of the NOR molecule, where the piperazine ring starts to open leading to the formation of

short-chained carbon molecules such as formates, as seen in Figure SM3. The subproduct 318.14 is also a variation of the first steps of the degradation of NOR, which can be the reason for the formation of fluoride ions at early stages. The subproduct 294.12 can be theoretically associated with an intermediate with the piperazine ring opened. The subproduct 251.08 can be associated with a molecule with the piperazine ring completely removed, leading to the formation of oxidized species derived from the nitrogen atoms allocated there, which can be related to the gradual evolution of ammonia observed in Figure SM3 and in the accumulation of nitrates as shown in Fig. 9. Finally, the intermediate of *m/z* 233.07, which is theoretically formed after the complete elimination of the piperazine ring and the defluorination of the NOR molecule, which can be confirmed due to the presence of fluorine and nitrates detected previously by ion chromatography.

3.3. Analysis of the energy consumption

To further analyze the mineralization of NOR, the efficiency of the system was described in Fig. 11, where the average values of the MCE, the energy consumption of the system and the extent of electrochemical consumption (estimated from Eqs. (1), (3) and (4), respectively) are shown for both electrodes, the BWO-BCE and BFO-BCE. MCE evolution with time was shown in Fig. 11a for the BWO-BCE, where an initial increase up to 15% at 60 min is observed, and a later slow decrease to 10%. The MCE average values (Fig. 11b) for the BWO-BCE at 8.33 mA·cm^{-2} are 11.82% under light exposure and 12.4% without it, which means a difference of 4.66%, an expected result taking under consideration the small effect of light seen in previous analysis at this current density, while the BFO-BCE presented 6.72% in presence of light and 5.83% in absence of it, with light having a slight effect over the MCE at this current density, as observed in Fig. 3. For 25 mA·cm^{-2} the values of MCE were always higher under light application, as expected since at this current density the light had a greater effect, whereas for the BFO-BCE, even though it had a better performance under light exposure, the improvement was less noticeable. This improvement under light exposure is related, as it has been stated before, to the higher formation of free radicals like ${}^{\cdot}OH$, SO$_4^{\cdot -}$ or O$_2^{\cdot -}$ that enhance the mineralization at the same applied current.

The energy consumption, whose instant values for the BWO-BCE are shown in Fig. 11c, indicate that almost steady values were obtained during all the experiment with little effect of light at low current densities, which aligns with that observed during the LSV analysis. Average values of energy consumed, shown in Fig. 11d, have a similar behavior as the MCE for both electrodes, where light had a positive effect in almost every scenario, but for the BWO-BCE at 8.33 mA·cm^{-2} no effect was observed (values were 897.52 kWh·kgTOC^{-1} and 907.58 kWh·kgTOC^{-1} in presence and absence of light). For the BWO-BCE, at 25 mA·cm^{-2} the average values were 5250.09 kWh·kgTOC^{-1} and 6124.66 kWh·kgTOC^{-1} in presence and absence of light, respectively. For both electrodes, increasing the current density increases the cell voltage, leading to the concomitant increase of energy consumption. Light reduces the cell voltage and, consequently, it reduces the energy consumption as seen.

The extent of electrochemical combustion calculated from Eq. (4) is shown in Fig. 11e for both electrodes. Light had little effect at low current densities but at higher current densities the BWO-BCE showed a better performance under light application (values closer to 1), which means that more degraded NOR could be also mineralized, corroborating what was previously observed in Fig. 3.

Electrodes with similar characteristics under similar testing conditions achieved values of the same order of magnitude. For instance, in the degradation of phenol, electrodes which consisted of a Ti mesh (M) covering an Sb-SnO$_2$ (M-SnO$_2$) anode presented a similar evolution trend for the MCE, with maximum values at the beginning and a later decrease with time. These values ranged between 20% and 15% at 10 mA·cm^{-2} in absence of light [51]. Also, a mixed metal-oxide

electrode under light exposure and 30 mA·cm^{-2} used for the degradation of ofloxacin, achieved MCE values of 30% which decreased during the first 60 min to around 7.5%, and then more gradually up to 2.5% after 4 h. Also, energy consumption values achieved were around 2500 kWh·kgTOC^{-1} after 4 h [52].

4. Conclusions

Bi$_2$WO$_6$ was successfully synthesized and adhered to the Sb-SnO$_2$ electrode via dip-coating, making a viable photoanode, the BWO-BCE, which was compared in different aspects with the BFO-BCE, another bismuth-based material, and with the BCE.

LSV experiments for the BWO-BCE showed its improvement with light, which presented a higher current density for the same applied potential. Also, photocurrent analysis of both electrodes, showed that the performance of the BWO-BCE improved at higher current densities and that of the BFO-BCE at lower current densities. This was further confirmed with the light pulsed chronoamperometries. Also, EIS showed an improvement of the BWO-BCE as the applied potential increased, reducing its charge transfer resistance. The comparison of the BWO-BCE with the BCE and BFO-BCE at + 1 V over the OCP showed a clear improvement when working with this photoanode at higher current densities.

Photoelectrooxidation experiments showed an improvement in the degradation of NOR of around 40% for both materials at 8.33 mA·cm^{-2} in relation to the BCE, but none at 25 mA·cm^{-2}, whereas in the mineralization the opposite occurred, obtaining improvements at 25 mA·cm^{-2} of 36% (BWO-BCE) and 28% (BFO-BCE). Also, for the BFO-BCE, light had a notable effect during all the degradation experiments at all current densities, especially at medium values. For the BWO-BCE at higher current densities the light effect was more noticeable and had a greater effect in the mineralization but almost negligible in the degradation.

The detection of formate indicated a proper oxidation of the NOR molecule, with higher concentrations at lower current densities for the BWO-BCE due to lower mineralization capability. For ammonia, at higher current densities the amount achieved was greater, due to a faster degradation of the NOR molecule, where light showed an increased elimination of ammonia, thanks to a higher oxidation. Fluorine content showed no major differences under light application or current density for both electrodes. Nitrate content was higher in presence of light due to higher generation of oxidizing species at both current densities and for both electrodes. However, there was a big effect of current density, doubling its concentration at high current density values, due to a greater degradation of the NOR molecule at high current densities. Also, the BFO-BCE presented greater concentrations than the BWO-BCE at both current densities. The presence of persulfates also indicated an oxidation of the supporting electrolyte, in a lower concentration when light was applied probably due to their activation. Also, the BWO-BCE presented greater amounts of persulfates, which is related to a higher toxicity.

MCE values indicated a better efficiency for the BWO-BCE at low current density, but less impactful at higher current densities. Energy consumption also showed slightly lower values for the BWO-BCE at 8.33 mA·cm^{-2}, but greater at 25 mA·cm^{-2}, where light reduced the energy consumption. Light had no effect on the extent of electrochemical combustion at low current densities for both electrodes, especially the BWO-BCE, however with light more degraded NOR was being mineralized for the BWO-BCE anode.

CRediT authorship contribution statement

The first author, Carlos Domingo Torner, is responsible for the methodology and the development of the experimental section. Manuel Cesar Martí-Calatayud is responsible for writing the original draft of the paper. The corresponding author, Montserrat García-Gabaldón, is responsible for the supervision and the planification of the research

activity. Sergio Mestre is responsible for the manufacture of the electrodes tested in this work. Valentín Pérez-Herranz is responsible for the funding acquisition.

Declaration of Competing Interest

The authors declare that they have no known competing financial interests or personal relationships that could have appeared to influence the work reported in this paper.

Data availability

The authors are unable or have chosen not to specify which data has been used.

Appendix A. Supporting information

Supplementary data associated with this article can be found in the online version at doi:10.1016/j.jece.2023.110616.

References

[1] C. Mutuku, Z. Gazdag, S. Melegh, Occurrence of antibiotics and bacterial resistance genes in wastewater: resistance mechanisms and antimicrobial resistance control approaches, World J. Microbiol. Biotechnol. 38 (2022) 1–27, https://doi.org/10.1007/s11274-022-03334-0.

[2] K. Tiseo, L. Huber, M. Gilbert, T.P. Robinson, T.P.Van Boeckel, Global trends in antimicrobial use in food animals from 2017 to 2030, Antibiotics 9 (2020) 1–14, https://doi.org/10.3390/antibiotics9120918.

[3] P. Kairigo, E. Ngumba, L.R. Sundberg, A. Gachanja, T. Tuhkanen, Occurrence of antibiotics and risk of antibiotic resistance evolution in selected Kenyan wastewaters, surface waters and sediments, Sci. Total Environ. 720 (2020), 137580, https://doi.org/10.1016/j.scitotenv.2020.137580.

[4] F. Hernández, N. Calisto-Ulloa, C. Gómez-Fuentes, M. Gómez, J. Ferrer, G. González-Rocha, H. Bello-Toledo, A.M. Botero-Coy, C. Boix, M. Ibáñez, M. Montory, Occurrence of antibiotics and bacterial resistance in wastewater and sea water from the Antarctic, J. Hazard. Mater. 363 (2019) 447–456, https://doi.org/10.1016/j.jhazmat.2018.07.027.

[5] L. Foyle, M. Burnett, A. Creaser, R. Hens, J. Keough, L. Madin, R. Price, H. Smith, S. Stone, R.T. Kinobe, Prevalence and distribution of antimicrobial resistance in effluent wastewater from animal slaughter facilities: A systematic review, Environ. Pollut. 318 (2023), 120848, https://doi.org/10.1016/j.envpol.2022.120848.

[6] M.C. Danner, A. Robertson, V. Behrends, J. Reiss, Antibiotic pollution in surface fresh waters: Occurrence and effects, Sci. Total Environ. 664 (2019) 793–804, https://doi.org/10.1016/j.scitotenv.2019.01.406.

[7] A.J. dos Santos, M.S. Kronka, G.V. Fortunato, M.R.V. Lanza, Recent advances in electrochemical water technologies for the treatment of antibiotics: A short review, Curr. Opin. Electrochem 26 (2021), 100674, https://doi.org/10.1016/j.coelec.2020.100674.

[8] O.M. Cornejo, M.F. Murrieta, L.F. Castañeda, J.L. Nava, Characterization of the reaction environment in flow reactors fitted with BDD electrodes for use in electrochemical advanced oxidation processes: A critical review, Electrochim. Acta 331 (2020), https://doi.org/10.1016/j.electacta.2019.135373.

[9] Y. Yang, Recent advances in the electrochemical oxidation water treatment: Spotlight on byproduct control, Front. Environ. Sci. Eng. 14 (2020), https://doi.org/10.1007/s11783-020-1264-7.

[10] P.J. Espinoza-Montero, P. Alulema-Pullupaxi, B.A. Frontana-Uribe, C.E. Barrera-Diaz, Electrochemical production of hydrogen peroxide on Boron-Doped diamond (BDD) electrode, Curr. Opin. Solid State Mater. Sci. 26 (2022), 100988, https://doi.org/10.1016/j.cossms.2022.100988.

[11] A. Rahmani, A. Shabanloo, N. Shabanloo, A mini-review of recent progress in lead dioxide electrocatalyst for degradation of toxic organic pollutants, Mater. Today Chem. 27 (2023), 101311, https://doi.org/10.1016/j.mtchem.2022.101311.

[12] A. Rahmani, A. Shabanloo, N. Shabanloo, Z. Torkshavand, A. Dargahi, A. Ansari, The integration of PbO$_2$-based EAOPs with other advanced oxidation processes for improved treatment of water and wastewater, Curr. Opin. Electrochem 37 (2023), 101204, https://doi.org/10.1016/j.coelec.2022.101204.

[13] A. Rahmani, A. Ansari, A. Seid-Mohammadi, M. Leili, D. Nematollahi, A. Shabanloo, Bismuth-doped 3D carbon felt/PbO$_2$ electrocatalyst for degradation of diuron herbicide and improvement of pesticide wastewater biodegradability,

J. Environ. Chem. Eng. 11 (2023), 109118, https://doi.org/10.1016/j.jece.2022.109118.

[14] J. Mora-Gomez, E. Ortega, S. Mestre, V. Pérez-Herranz, M. García-Gabaldón, Electrochemical degradation of norfloxacin using BDD and new Sb-doped SnO$_2$ ceramic anodes in an electrochemical reactor in the presence and absence of a cation-exchange membrane, Sep. Purif. Technol. 208 (2019) 68–75, https://doi.org/10.1016/j.seppur.2018.05.017.

[15] J. Carrillo-Abad, J. Mora-Gómez, M. García-Gabaldón, S. Mestre, V. Pérez-Herranz, Comparison between an electrochemical reactor with and without membrane for the nor oxidation using novel ceramic electrodes, J. Environ. Manag. 268 (2020), https://doi.org/10.1016/j.jenvman.2020.110710.

[16] C. Domingo-Torner, M. García-Gabaldón, M.C. Martí-calatayud, S. Mestre, V. Pérez-Herranz, Norfloxacin mineralization under light exposure using Sb–SnO$_2$ ceramic anodes coated with BiFeO$_3$ photocatalyst, Chemosphere 313 (2023), 137518, https://doi.org/10.1016/j.chemosphere.2022.137518.

[17] M.R. Al-Mamun, S. Kader, M.S. Islam, M.Z.H. Khan, Photocatalytic activity improvement and application of UV-TiO$_2$ photocatalysis in textile wastewater treatment: A review, J. Environ. Chem. Eng. 7 (2019), https://doi.org/10.1016/j.jece.2019.103248.

[18] B.O. Orimolade, A.O. Idris, U. Feleni, B. Mamba, Recent advances in degradation of pharmaceuticals using Bi$_2$WO$_6$ mediated photocatalysis – A comprehensive review, Environ. Pollut. 289 (2021), 117891, https://doi.org/10.1016/j.envpol.2021.117891.

[19] A. Gordanshekan, S. Arabian, A.R. Solaimany Nazar, M. Farhadian, S. Tangestaninejad, A comprehensive comparison of green Bi$_2$WO$_6$/g-C$_3$N$_4$ and Bi2WO6/TiO$_2$ S-scheme heterojunctions for photocatalytic adsorption/degradation of Cefixime, Artif. Neural Netw., Degrad. Pathw., to, Chem. Eng. J. 451 (2023), 139067, https://doi.org/10.1016/j.cej.2022.139067.

[20] T. Chen, L. Liu, C. Hu, H. Huang, Recent advances on Bi$_2$WO$_6$-based photocatalysts for environmental and energy applications, Chin. J. Catal. 42 (2021) 1413–1438, https://doi.org/10.1016/S1872-2067(20)63769-X.

[21] Y. Jing, A. Fan, J. Guo, T. Shen, S. Yuan, Y. Chu, Synthesis of an ultrathin MnO$_2$ nanosheet-coated Bi$_2$WO$_6$ nanosheet as a heterojunction photocatalyst with enhanced photocatalytic activity, Chem. Eng. J. 429 (2022), 132193, https://doi.org/10.1016/j.cej.2021.132193.

[22] H. Ait Ahsaine, A. BaQais, M. Arab, B. Bakiz, A. Benlhachemi, Synthesis and Electrocatalytic Activity of Bismuth Tungstate Bi$_2$WO$_6$ for Rhodamine B Electro-Oxidation, Catalysts 12 (2022) 1335, https://doi.org/10.3390/catal12111335.

[23] J. Ke, H. Zhou, J. Liu, X. Duan, H. Zhang, S. Liu, S. Wang, Crystal transformation of 2D tungstic acid H$_2$WO$_4$ to WO$_3$ for enhanced photocatalytic water oxidation, J. Colloid Interface Sci. 514 (2018) 576–583, https://doi.org/10.1016/j.jcis.2017.12.066.

[24] K. Qin, Q. Zhao, H. Yu, X. Xia, J. Li, S. He, L. Wei, T. An, A review of bismuth-based photocatalysts for antibiotic degradation: Insight into the photocatalytic degradation performance, pathways and relevant mechanisms, Environ. Res. 199 (2021), 111360, https://doi.org/10.1016/j.envres.2021.111360.

[25] T. Chankhanittha, V. Somaudon, T. Photiwat, S. Youngme, K. Hemavibool, S. Nanan, Enhanced photocatalytic performance of ZnO/Bi$_2$WO$_6$ heterojunctions toward photodegradation of fluoroquinolone-based antibiotics in wastewater, J. Phys. Chem. Solids 153 (2021), 109995, https://doi.org/10.1016/j.jpcs.2021.109995.

[26] P. Kumar, S. Verma, N.Č. Korošin, B. Žener, U.L. Štangar, Increasing the photocatalytic efficiency of ZnWO$_4$ by synthesizing a Bi$_2$WO$_6$/ZnWO$_4$ composite photocatalyst, Catal. Today 397–399 (2022) 278–285, https://doi.org/10.1016/j.cattod.2021.09.012.

[27] X. Yuan, D. Shen, Q. Zhang, H. Zou, Z. Liu, F. Peng, Z-scheme Bi$_2$WO$_6$/CuBi$_2$O$_4$ heterojunction mediated by interfacial electric field for efficient visible-light photocatalytic degradation of tetracycline, Chem. Eng. J. 369 (2019) 292–301, https://doi.org/10.1016/j.cej.2019.03.082.

[28] M. Zargazi, M.H. Entezari, Anodic electrophoretic deposition of Bi$_2$WO$_6$ thin film: high photocatalytic activity for degradation of a binary mixture, Appl. Catal. B Environ. 242 (2019) 507–517, https://doi.org/10.1016/j.apcatb.2018.09.093.

[29] J. Mora-Gómez, M. García-Gabaldón, E. Ortega, M.J. Sánchez-Rivera, S. Mestre, V. Pérez-Herranz, Evaluation of new ceramic electrodes based on Sb-doped SnO$_2$ for the removal of emerging compounds present in wastewater, Ceram. Int. 44 (2018) 2216–2222, https://doi.org/10.1016/j.ceramint.2017.10.178.

[30] T. Droguett, J. Mora-Gómez, M. García-Gabaldón, E. Ortega, S. Mestre, G. Cifuentes, V. Pérez-Herranz, Electrochemical Degradation of Reactive Black 5 using two-different reactor configuration, Sci. Rep. 10 (2020) 1–11, https://doi.org/10.1038/s41598-020-61501-5.

[31] J. Mora-Gómez, M. García-Gabaldón, J. Carrillo-Abad, M.T. Montañés, S. Mestre, V. Pérez-Herranz, Influence of the reactor configuration and the supporting electrolyte concentration on the electrochemical oxidation of Atenolol using BDD and SnO$_2$ ceramic electrodes, Sep. Purif. Technol. 241 (2020), https://doi.org/10.1016/j.seppur.2020.116684.

[32] A. El-Ghenymy, C. Arias, P.L. Cabot, F. Centellas, J.A. Garrido, R.M. Rodríguez, E. Brillas, Electrochemical incineration of sulfanilic acid at a boron-doped diamond anode, Chemosphere 87 (2012) 1126–1133, https://doi.org/10.1016/j.chemosphere.2012.02.006.

[33] J. Carrillo-Abad, J. Mora-Gómez, M. García-Gabaldón, M.T. Montañés, S. Mestre, V. Pérez-Herranz, Enhanced Atenolol oxidation by ferrites photoanodes grown on

ceramic SnO$_2$-Sb$_2$O$_3$ anodes, J. Alloy. Compd. 908 (2022), 164629, https://doi.org/10.1016/j.jallcom.2022.164629.

[34] S.W. da Silva, E.M.O. Navarro, M.A.S. Rodrigues, A.M. Bernardes, V. Pérez-Herranz, The role of the anode material and water matrix in the electrochemical oxidation of norfloxacin, Chemosphere 210 (2018) 615–623, https://doi.org/10.1016/j.chemosphere.2018.07.057.

[35] J. Mora-Gómez, S. Escribá-Jiménez, J. Carrillo-Abad, M. García-Gabaldón, M.T. Montañés, S. Mestre, V. Pérez-Herranz, Study of the chlorfenvinphos pesticide removal under different anodic materials and different reactor configuration, Chemosphere 290 (2022), https://doi.org/10.1016/j.chemosphere.2021.133294.

[36] R.S. Roth, T. Negas, L.P. Cook, Phase Diagr. Ceram. Vol. IV (1981).

[37] H. Wang, L. Zhang, Z. Chen, J. Hu, S. Li, Z. Wang, J. Liu, X. Wang, Semiconductor heterojunction photocatalysts: Design, construction, and photocatalytic performances, Chem. Soc. Rev. 43 (2014) 5234–5244, https://doi.org/10.1039/c4cs00126e.

[38] M.P. Ravikumar, S. Bharathkumar, B. Urupalli, M.K. Murikinati, S.M. Venkatakrishnan, S. Mohan, Insights into the Photocatalytic Memory Effect of Magneto- Plasmonic Ag−Fe$_3$O$_4$@TiO$_2$ Ternary Nanocomposites for Dye degradation and H$_2$ Production under light and dark Conditions, Energy Fuels 36 (2022) 11503–11514, https://doi.org/10.1021/acs.energyfuels.2c01563.

[39] S.H. Liu, W.T. Tang, P.H. Chou, Microwave-assisted synthesis of triple 2D g-C$_3$N$_4$/Bi$_2$WO$_6$/rGO composites for ibuprofen photodegradation: Kinetics, mechanism and toxicity evaluation of degradation products, Chem. Eng. J. 387 (2020), 124098, https://doi.org/10.1016/j.cej.2020.124098.

[40] K.C. de Freitas Araújo, D.R. da Silva, E.V. dos Santos, H. Varela, C.A. Martínez-Huitle, Investigation of persulfate production on BDD anode by understanding the impact of water concentration, J. Electroanal. Chem. 860 (2020), 113927, https://doi.org/10.1016/j.jelechem.2020.113927.

[41] Y. Wu, X. Zhao, J. Tian, S. Liu, W. Liu, T. Wang, Heterogeneous catalytic system of photocatalytic persulfate activation by novel Bi$_2$WO$_6$ coupled magnetic biochar for degradation of ciprofloxacin, Colloids Surf. A Physicochem. Eng. Asp. 651 (2022), 129667, https://doi.org/10.1016/j.colsurfa.2022.129667.

[42] J. Li, H. Wang, N. Reddy, Z. Zhu, J. Zheng, W. Wang, B. Liu, C. Hu, MOFFeCo/B-CN composites achieve efficient degradation of antibiotics in a non-homogeneous concurrent photocatalytic-persulfate activation system, Sci. Total Environ. 858 (2023), 159795, https://doi.org/10.1016/j.scitotenv.2022.159795.

[43] I.M.D. Gonzaga, A.R. Dória, A. Moratalla, K.I.B. Eguiluz, G.R. Salazar-Banda, P. Cañizares, M.A. Rodrigo, C. Saez, Electrochemical systems equipped with 2D and 3D microwave-made anodes for the highly efficient degradation of antibiotics in urine, Electrochim. Acta 392 (2021), 139012, https://doi.org/10.1016/j.electacta.2021.139012.

[44] K.N. Parra, S. Gul, J.M. Aquino, D.W. Miwa, A.J. Motheo, Electrochemical degradation of tetracycline in artificial urine medium, J. Solid State Electrochem 20 (2016) 1001–1009, https://doi.org/10.1007/s10008-015-2833-8.

[45] C.A.G. Bezerra, J.P.T. da, S. Santos, G.G. Bessegato, C.L. de Paiva e Silva Zanta, V. Del Colle, G. Tremiliosi-Filho, Photo- and electro-oxidation of tetracycline hydrochloride on self-doped titanium dioxide nanotubes modified by Pt sub-monolayers, Electrochim. Acta 404 (2022), https://doi.org/10.1016/j.electacta.2021.139712.

[46] Y. Niu, Y. Yin, R. Xu, Z. Yang, J. Wang, D. Xu, Y. Yuan, J. Han, H. Wang, Electrocatalytic oxidation of low concentration cefotaxime sodium wastewater using Ti/SnO$_2$–RuO$_2$ electrode: Feasibility analysis and degradation mechanism, Chemosphere 297 (2022), 134146, https://doi.org/10.1016/j.chemosphere.2022.134146.

[47] L. Franzen Ramos, S.W. da Silva, D.E. Schneider, M.A.S. Rodrigues, A.M. Bernardes, Mineralization of erythromycin by UV-based and electro-oxidation processes, J. Water Process Eng. 33 (2020), 101039, https://doi.org/10.1016/j.jwpe.2019.101039.

[48] A. Balseviciute, M.C. Martí-Calatayud, V. Pérez-Herranz, S. Mestre, M. García-Gabaldón, Novel Sb-doped SnO$_2$ ceramic anode coated with a photoactive BiPO$_4$ layer for the photoelectrochemical degradation of an emerging pollutant, Chemosphere 335 (2023), 139173, https://doi.org/10.1016/J.CHEMOSPHERE.2023.139173.

[49] C. Guo, S. Gao, J. Lv, S. Hou, Y. Zhang, J. Xu, Assessing the photocatalytic transformation of norfloxacin by BiOBr/iron oxides hybrid photocatalyst: Kinetics, intermediates, and influencing factors, Appl. Catal. B Environ. 205 (2017) 68–77, https://doi.org/10.1016/j.apcatb.2016.12.032.

[50] L. Tang, J. Wang, G. Zeng, Y. Liu, Y. Deng, Y. Zhou, J. Tang, J. Wang, Z. Guo, Enhanced photocatalytic degradation of norfloxacin in aqueous Bi$_2$WO$_6$ dispersions containing nonionic surfactant under visible light irradiation, J. Hazard. Mater. 306 (2016) 295–304, https://doi.org/10.1016/j.jhazmat.2015.12.044.

[51] L. Huang, D. Li, J. Liu, L. Yang, C. Dai, N. Ren, Y. Feng, Construction of TiO$_2$ nanotube clusters on Ti mesh for immobilizing Sb-SnO$_2$ to boost electrocatalytic phenol degradation, J. Hazard. Mater. 393 (2020), https://doi.org/10.1016/j.jhazmat.2020.122329.

[52] R. Antonelli, G.R.P. Malpass, M.G. Carlos da Silva, M.G.A. Vieira, Ofloxacin degradation in chloride-containing medium by photo-assisted sonoelectrochemical process using a mixed metal oxide anode, J. Environ. Chem. Eng. 10 (2022), 107174, https://doi.org/10.1016/j.jece.2022.107174.